IET Microwaves, Antennas & Propagation

WILEY

The Institution of Engineering and Technology

ORIGINAL RESEARCH OPEN ACCESS

A Feasibility Study to Practically Implement a High-Performance Circularly Polarised Antenna Array for Point-to-Point Wireless Communication

Mahdi Parvaneh[1] | Hassan Zakeri[1] | Gholamreza Moradi[1] | Mohammad Alibakhshikenari[2,3] | Bandar Alshammari[4] | Chan Hwang See[5] | Bal Virdee[6] | Symon K. Podilchak[4,7] | Ernesto Limiti[8]

[1]Department of Electrical Engineering, Amirkabir University of Technology, Tehran, Iran | [2]LERO, the Research Ireland Centre for Software, College of Science and Engineering, School of Computer Science, University of Galway, Galway, Ireland | [3]Department of Electrical and Electronics Engineering, Dogus University, Istanbul, Türkiye | [4]Institute of Imaging, Data, and Communications (IDCOM), The University of Edinburgh, Edinburgh, UK | [5]School of Engineering and the Built Environment, Edinburgh Napier University, Edinburgh, UK | [6]Center for Communications Technology, London Metropolitan University, London, UK | [7]Institute of Sensors, Signals, and Systems (ISSS), Heriot-Watt University, Edinburgh, UK | [8]Department of Electronic Engineering, University of Rome Tor Vergata, Rome, Italy

Correspondence: Mohammad Alibakhshikenari (mohammad.alibakhshikenari@universityofgalway.ie)

Received: 26 November 2024 | **Revised:** 15 December 2025 | **Accepted:** 19 December 2025

Handling Editor: Xun Luo

Keywords: antenna arrays | broadband antennas | microstrip lines | power dividers

ABSTRACT

This article presents the design, fabrication and experimental validation of a compact linear series-fed microstrip antenna array with dual circular polarisation (CP) capability. The proposed structure consists of a 4 × 4 slotted circular patch array excited via four microstrip lines using a coplanar proximity coupling technique. Dual-CP operation is achieved through two miniaturised and distinct microstrip power divider networks, enabling the generation of either left-hand or right-hand CP based on the excitation port. To maximise gain and efficiency, the design reduces feedline branching and employs optimised slotted patch elements, resulting in low power loss and high radiation efficiency. The antenna achieves a realised peak gain of 19.4 dBic across 12.2–12.7 GHz and a 3-dB axial ratio bandwidth from 11.9 to 13.1 GHz. Simulation and measurement results demonstrate excellent agreement. Thanks to its compact size, wide bandwidth, dual-CP functionality and high gain, the proposed antenna offers a promising solution for point-to-point wireless communication systems. Compared to existing multi- and single-layer microstrip-based CP arrays, this work introduces a simplified feed structure and improved performance, demonstrating clear advancement in antenna array design.

1 | Introduction

Wireless circular polarisation (CP) has gained considerable attention in modern communication systems because of its numerous advantages. Its ability to radiate in all planes increases the likelihood of establishing reliable links, particularly in dynamic environments. As a result, CP antennas help reduce multipath reflections, delay spread and polarisation mismatch losses, while allowing more flexible orientation between transmitting (Tx) and receiving (Rx) antennas [1–4]. These advantages make CP antennas highly suitable for a wide range of applications, including biomedical devices [5], wireless sensors [6], THz applications [7–9], energy harvesting [10], internet of things (IoT) [11] and in 5G/6G technologies [12–15].

CP antennas typically support either LHCP or RHCP. In many advanced wireless systems, the ability to support both is known as dual-CP and is especially valuable for improving link reliability and communication flexibility [16–19]. Dual-CP antennas also benefit from reduced susceptibility to multipath and Faraday rotation, leading to more consistent performance in complex environments [20–23].

A key design challenge in dual-CP antennas is achieving both LHCP and RHCP radiation in a compact form while allowing for polarisation selection. In Ref. [13], dual-CP is realised using two separate patch elements, which increases the size and complexity of the antenna, although it does improve isolation. More recent designs attempt to generate either LHCP or RHCP by exciting specific ports, which improves efficiency [24].

Despite these advances, mutual coupling or self-interference between the ports remains a critical limitation in dual-CP designs. This unwanted electromagnetic interaction degrades port isolation and overall radiation performance [25, 26].

According to the sequential rotation method, a low-cost single-layer dual-CP series-fed antenna is presented in Ref. [27]. Curved microstrip lines capable of being printed on a single PCB layer without any problems with manufacturing, assembly or processing provide the antenna's radiation elements. Because of this, although it has an axial ratio (AR) bandwidth of just about 10%.

Using circular grooves along with two orthogonal L-shaped feeders in the ground plane, producing RHCP and LHCP in the same frequency band is possible. Meanwhile, the efficiency of the CP antenna can be enhanced by suitably slotting and including parasitic components on the ground plane. By doing fabrication, the suggested antenna's gain decreases despite having a higher AR [28].

Furthermore, these designs may experience strong coupling between closely spaced patches, particularly when radiation occurs from both sides of the substrate—adversely affecting the axial ratio.

An alternative technique is the dual-CP travelling-wave series-fed array, using slotted circular patches and microstrip coupling [29, 30].

It has been demonstrated in Ref. [31] that if the feeding network can maintain the proper amplitude and phase over the frequency, the CP bandwidth (BW) in the axial broadside direction can be considerable. Nevertheless, the performance of the feeding network and the radiating devices limits the practical circular polarisation BW due to mutual coupling, magnitude errors, impedance mismatch and phase errors.

To achieve the appropriate phase shifting and power splitting among the radiating elements, researchers in Refs. [32, 33] propose using a series-fed network. The feed network is configured with an open ring structure.

The CP antennas proposed in Ref. [34] exhibited a limited axial ratio bandwidth (ARBW). In contrast, the antenna designed in Ref. [35] introduces a structure that increases the ARBW, but the gain is low. Researchers in Ref. [36], by analysing and comparing the structure by including or not the U slot, reached a result that a U slot shape would create a narrower ARBW. However, as demonstrated in Ref. [37], these structures are bulky, with 93 mm in length. A partly reflecting surface (PRS) is used at the top of the antenna in Ref. [38], which offers an alternative method for generating CP with a wide bandwidth. However, this design is extensive because of the necessary thickness.

Various feeding implementations are presented and compared in Refs. [39, 40]. It has been demonstrated that a hybrid ring-feeding network can produce good performance. However, because of the extremely short wavelength, the thick substrate height and high dielectric permittivity allow the realisation of more complex feeding structures with a small footprint [41, 42].

Placing radiating patches in proximity to power dividers and exciting them via electromagnetic coupling, rather than direct line feeds, presents notable advantages. Direct excitation often leads to resistive and impedance mismatch losses. In contrast, coupled feeding improves radiation efficiency [43]. This approach also enhances structural compactness, which is crucial for mm-wave communications, IoT devices and automotive radar systems [44–46]. The power divider network also helps maintain good impedance matching by ensuring uniform power distribution and reducing mismatch losses [47, 48]. The power divider network can improve impedance matching across an antenna array by adjusting coupling to each patch, reducing mismatch losses and ensuring uniform power distribution [49, 50].

This paper proposes a high-gain dual-CP series-fed microstrip patch array consisting of 16 circular slotted patches. Two compact 1-to-4 power divider networks are employed on either side of the array to generate both LHCP and RHCP modes, depending on the selected port. The remainder of the paper is organised as follows: Section 2 presents the theoretical background and design of the proposed antenna. Section 3 validates the design through simulation and experimental measurement of a fabricated prototype. Section 4 compares the results with those of related work. Finally, Section 5 summarises the key findings and conclusions of this study.

The proposed antenna is designed to maximise gain and minimise power loss by reducing the number of branching lines in the 1-to-4 power divider and utilising optimised slotted circular patch elements with high radiation efficiency. Its innovations include achieving compactness and simplicity while providing dual circular polarisation without relying on two separate 4 × 4 patch arrays, thereby ensuring high-gain radiation performance. Moreover, it effectively bridges the gap between theoretical performance and practical implementation, making it a highly suitable solution for high-performance wireless communication scenarios, particularly in point-to-point links such as satellite and microwave backhaul systems.

2 | Antenna Array Design and Discussion

The development of the proposed dual circularly polarised (dual-CP) antenna, as illustrated in Figure 1, progresses from a

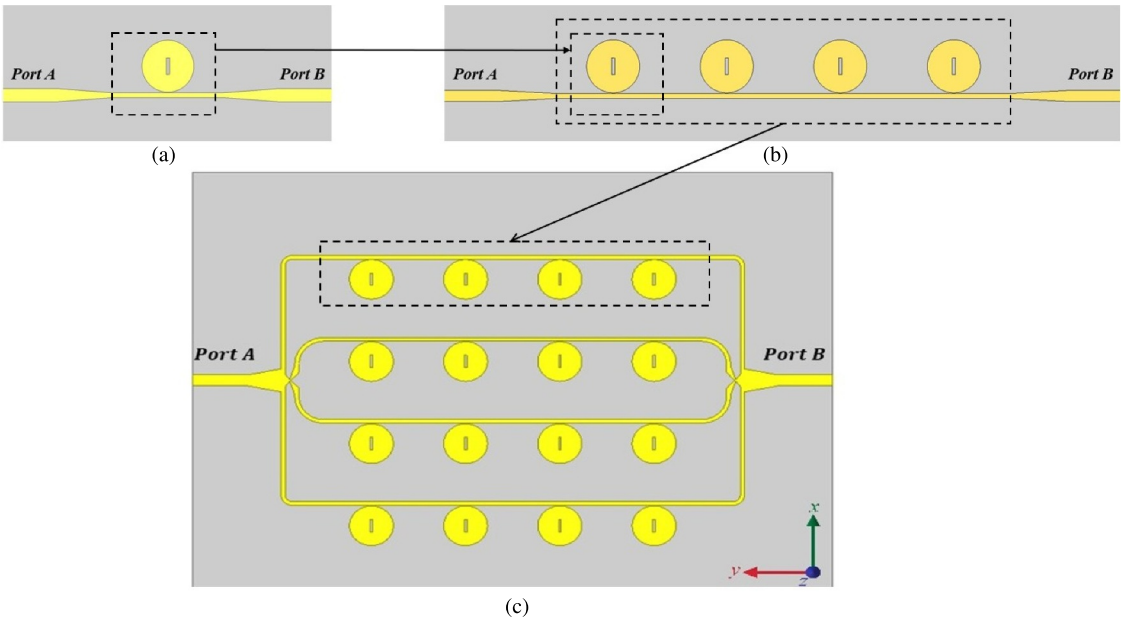

FIGURE 1 | The progression of the proposed dual-CP antenna structure: (a) single slotted circular patch element with coplanar microstrip feed, (b) single linear row of four circular patches excited via proximity coupling, and (c) complete 4 × 4 antenna array integrated with two compact power divider networks to achieve dual CP.

single radiating element to a complete array structure. The design consists of two key components: the power divider and the radiating patch array.

- Figure 1a shows a single slotted circular patch with a coplanar microstrip feed, serving as the fundamental radiating unit.
- Figure 1b presents a linear row of four circular patch elements, each excited via proximity coupling by a dedicated microstrip feed line element, which is critical for maintaining constructive interference in the main beam direction.
- Figure 1c displays the full 4 × 4 array configuration, incorporating two compact power divider networks on opposite sides. These enable dual-CP operation by selectively exciting the appropriate input port.

This step-by-step progression visually demonstrates the structural evolution and integration of the feed network with the radiating elements, highlighting how input power is distributed across the array to achieve efficient CP.

The substrate layer used in the antenna is Rogers RT/Duroid5880, with a dielectric constant of $\epsilon_r = 2.2$, a loss tangent of $\tan\delta = 0.0009$ and the substrate thickness (H) is 31 mil. Additionally, the proposed antenna's overall dimension is 125 × 90 mm^2. All simulation results shown in the following were performed with Ansys HFSS.

2.1 | Power Divider

The proposed antenna incorporates four parallel microstrip feeding lines, each designed to excite a linear array of radiating elements. To support this configuration, a four-way microstrip power divider was developed, as illustrated in Figure 2. The power distribution among the output lines can be adjusted by varying the width of the microstrip lines, allowing for flexible control of power ratios. The feed network adopts an intersection-style layout at the power-splitting junctions, which provides several design advantages:

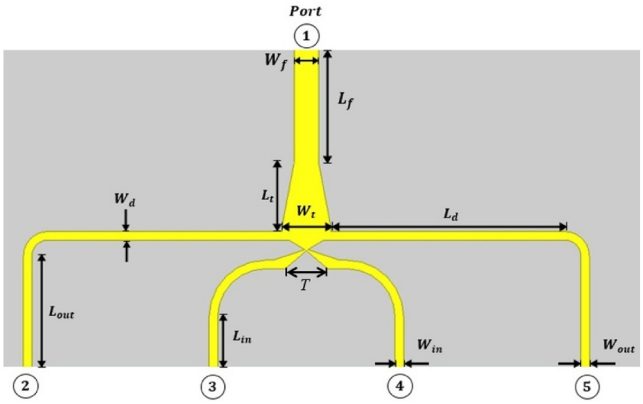

FIGURE 2 | Schematic of the proposed power divider (W_f = 2.4 mm, W_{in} = 0.8 mm, W_t = 4.6 mm, L_f = 10.8 mm, L_t = 6.45 mm, L_d = 22.4 mm, W_{out} = W_d = 0.8 mm, L_{in} = 4.35 mm, L_{out} = 10.45 mm, T = 2 mm.). T controls the junction overlap/transition length (effective impedance at the split), not the nominal physical widths of the branch lines.

- A compact footprint, reducing the overall layout area.
- A symmetrical structure, ensuring uniform amplitude and phase distribution across all four outputs.
- Lower transmission loss, due to the elimination of multi-stage splitters and reduced line lengths.

Despite its benefits, the intersection design requires careful attention during fabrication:

- High-precision etching is essential to maintain impedance continuity and minimise reflection.
- Corner tapering or rounding should be employed to prevent current crowding at junctions.
- Consistent trace width and substrate uniformity must be maintained to ensure accurate phase matching and stable network behaviour.

These considerations were addressed and optimised through full-wave electromagnetic simulations. The final layout was refined to ensure efficient power distribution and stable performance across the target frequency band.

The use of tapered structures in the feed lines helps reduce power reflection, thereby enhancing transmission efficiency [51, 52].

This technique enables a smooth transition between feed lines of varying widths and characteristic impedances. To ensure optimal performance, the taper dimensions were carefully optimised using full-wave electromagnetic simulations in Ansys HFSS, minimising reflections across the desired bandwidth. Importantly, the design employs a single-stage 1-to-4 power divider rather than a two-stage branching configuration (i.e., 1-to-2 followed by 2-to-4, as seen in Refs. [53, 54]. This decision was made to achieve a more compact layout, reduce space consumption and minimise transmission loss. As a result, we avoided using a multi-stage power divider while still maintaining equal phase and amplitude distribution across the outputs.

Due to the structural symmetry of the proposed power divider, the S-parameters conform to Equation (1)

$$\begin{aligned} |S_{21}| = |S_{51}| \;\&\; |S_{31}| = |S_{41}| \\ \angle S_{21} = \angle S_{51} \;\&\; \angle S_{31} = \angle S_{41} \end{aligned} \tag{1}$$

Equation (2) should be maintained in the design of a 1-to-4 power divider.

$$|S_{21}|^2 \simeq |S_{31}|^2 \tag{2}$$

Basic design improvement necessitates consideration of the phase difference between the ports ($|\angle S_{21} - \angle S_{31}|$ & $|\angle S_{51} - \angle S_{41}|$) over the frequency is not exceed 10° [55, 56].

The value of $\left(\sum_{i=2}^{5} S_{i1}^2\right) \times P_{\text{in}}$ demonstrates the total received power to the output ports, where P_{in} is the input power of the power divider. As a result, the value of $\left(1 - \sum_{i=1}^{5} S_{i1}^2\right) \times P_{\text{in}}$ demonstrates the power loss in the power divider. The total value of received power to the output ports from 11.5 to 13.5 GHz is shown in Figure 3, which demonstrates the proper bandwidth of the divider.

As a result, this condition is established only for a specific frequency range to maintain the proper phase difference between the output ports. As demonstrated in Figure 4a, according to the power divider design, the rate of change of $|\angle S_{21} - \angle S_{31}|$ and $|\angle S_{51} - \angle S_{41}|$ values are linear with frequency. Hence, the beginning and end of the frequency range are equal to 12.19 and 12.97 GHz, respectively, which is more significant than the desired frequency range (12.2–12.7 GHz).

In Figure 4a, the inter-output phase error $|\angle S_{21} - \angle S_{31}|$ and $|\angle S_{51} - \angle S_{41}|$ stays within 10° from 12.19 to 12.97 GHz; $\Delta f \approx$

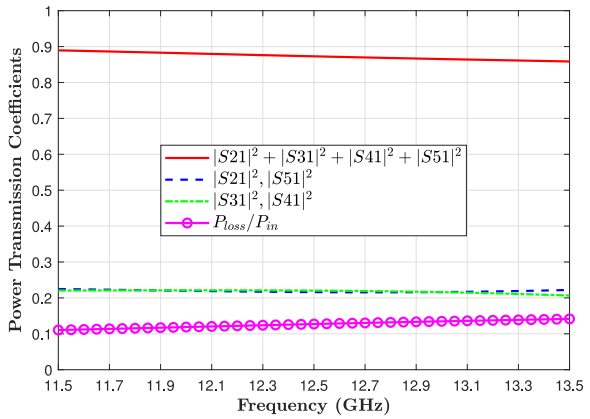

FIGURE 3 | The proposed 1-to-4 power divider transmission coefficients.

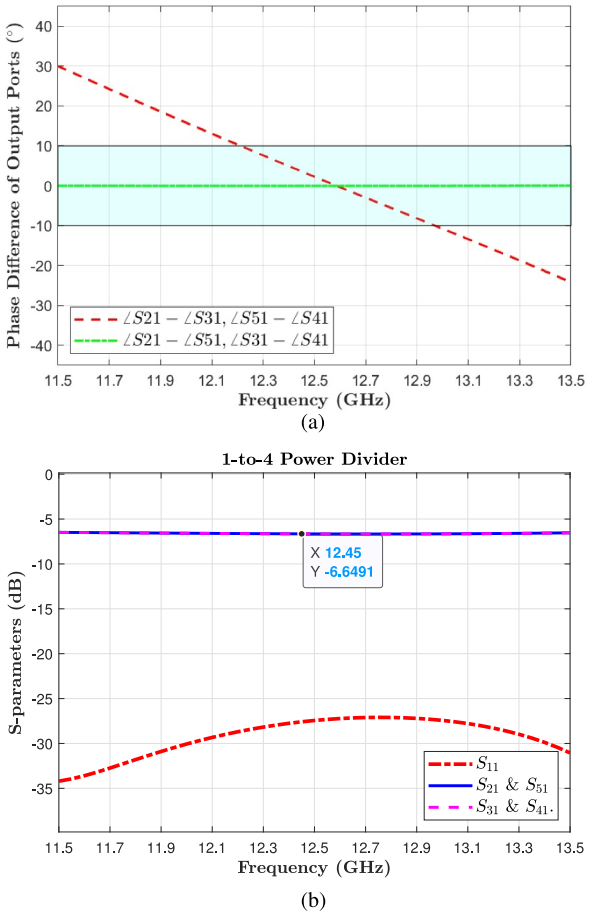

FIGURE 4 | (a) Phase difference of output ports in the proposed 1-to-4 power divider, and (b) S-parameters of the proposed power divider.

0.78 GHz (≈ 6.3% w.r.t. 12.45 GHz), which specifies the equal-phase window of the divider, not a hard limit on the antenna's CP bandwidth. The usable operating band of the complete antenna is defined by the overlap of (i) input matching $|S_{AA}|$, $|S_{BB}| < -10$ dB, (ii) port isolation $|S_{AB}|$, $|S_{BA}| < -12$dB, and (iii) AR < 3 dB (see Figure 21). Applying these criteria yields 12.2–12.7 GHz (≈ 4%). Note that the radiating section itself supports a wider 3-dB AR bandwidth of 11.9–13.1 GHz, indicating that the feed's 10° phase window is not the bottleneck.

Figure 4b demonstrates that the transmission in each line is about −6.61 dB; therefore, the insertion loss is 0.61 dB (which means it is between the 0.5 dB and 0.7 [57–60]). As a result, this power divider helps to reduce the amount of loss in all the proposed structures.

The amount loss of the power divider (P_{loss}) is calculated by the following equation:

$$P_{\text{loss}} = \left(1 - \sum_{i=2}^{5} |S_{i1}|^2\right) \times P_{\text{in}} \tag{3}$$

2.2 | Radiating Patch Elements

As illustrated in Figure 5, the proposed antenna consists of four parallel feed lines, each connected to a linear array of four circular patch elements. These patch elements support dual-CP, either LHCP or RHCP, depending on whether the beginning or end of the corresponding microstrip feed line is excited. To enhance CP performance, each circular patch is designed with a central slot, which introduces the necessary perturbation for improved axial ratio and polarisation purity.

In Figure 5, the proposed patch design employs a vertical slot aligned along the *y*-axis at the centre of each circular patch. This vertical slot differs from a slanted slot (e.g., with a 45° inclination) in several ways:

- It excites orthogonal modes primarily along the Cartesian axes, which effectively generates CP with reduced complexity.
- It maintains geometric symmetry, which benefits radiation uniformity and improves isolation between LHCP and RHCP ports in a dual-CP system.

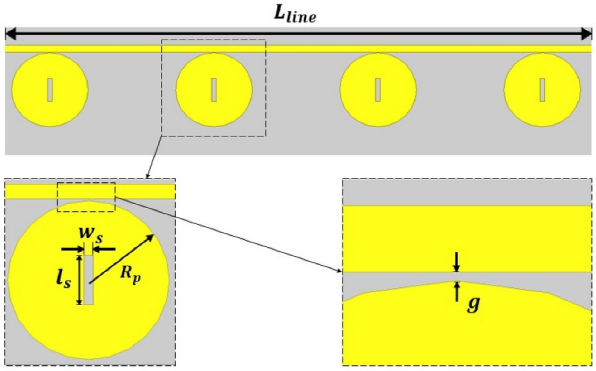

FIGURE 5 | Schematic of a single row coplanar microstrip feeding line (L_{line} = 65 mm, R_p = 4.3 mm, w_s = 0.5 mm, l_s = 2.7 mm, g = 0.1 mm).

- It simplifies fabrication by allowing straightforward alignment and consistent etching across multiple patch elements. By contrast, a slanted slot may provide broader axial ratio bandwidth through stronger hybrid mode excitation but requires more delicate tuning and careful layout.

In our design, the vertical slot was optimised via full-wave simulation to provide strong CP and maintain compact and symmetric antenna geometry.

The rectangular slot in the circular patch's centre creates a small perturbation by altering the symmetry and generating the necessary phase difference between the two orthogonal modes. The dimensions and orientation of the slot can be optimised to control the phase shift.

The circular patch with radius R_p is illustrated in Figure 5, whose radiating structure is comprised of a rectangular slot with a size of $l_s \times w_s$ precisely in the middle of the circular patch.

It is essential to consider that the coupling of the electrical field on the patch elements is directly proportional to the width of the line. Therefore, increasing the width of the line increases the electrical field on the patches, too. However, for proper coupling, the gap size must be lower than half the width of the line [61, 62].

Each patch gradually harvests a portion of the power from the guided wave as it moves from an excited port to the other end using the coplanar proximity coupling.

The captured energy plays a crucial role in exciting the fundamental TM^z_{110} mode in the patch, a critical factor in causing radiation with CP. The travelling wave, related to Lenz's law, is opposite to the CP's handedness. The condition for each element to be in-phase must be satisfied when broadside radiation is required.

It is important to note that when the spacing between elements is equal to one λ_g, the waves generated by each element will be in phase in a specific direction.

As a result, there is one guided wavelength (λ_g) between the adjacent elements in the area. The guided wavelength at the substrate's central frequency (12.45 GHz) is 17.62 mm. After the simulations in Ansys HFSS, the optimised distance between the radiation patch elements in the direction of x and y equals 17.8 and 18.4 mm, respectively.

These findings can be practically applied to calculate the effective radius R_p of a circular patch operating in the TM^z_{110} mode at frequency f_{110} using Equation (4). This calculation can determine the best radius value for a slotted circular-shaped patch.

$$f_{110} = \frac{\chi \times c}{2\pi R_p \sqrt{\mu_0 \epsilon_0} \sqrt{\epsilon_r}} \tag{4}$$

where χ is the m^{th} zero of the derivative of the Bessel function of order n (i.e., $J'_n(ka)$, and $\chi_{110} = 1.8412$ for the TM^z_{110} or quasi TM^z_{110} mode), also, c, f_{110}, μ_0, ϵ_0, and ϵ_r are the velocity of light in free space, target resonance frequency, free space permeability, free

space permittivity and the relative permittivity for the substrate of the circular patch, respectively.

The slot at the patch centre was introduced to allow for more flexibility in improving CP performance. Broadside radiation with RHCP could be generated at the nominal frequency of 12.45 GHz if Port A is the only port stimulated. However, LHCP could be generated by the excitation of Port B.

The antenna impedance BW is limited by the two ports of a two-port device having sufficient isolation (transmission coefficient less than −12 dB) between them. This means that the patch elements must catch and radiate almost all of the power of the directed travelling waves before they reach the other port. Therefore, fewer array elements will be permitted, and the coplanar proximity coupling strength between the elements and the microstrip feeding line will be stronger.

Establishing a small gap between the line and the circular patch improves the proximity coupling, enabling high antenna efficiency and acceptable operating BW with few array elements. As a result, the energy radiation rate along the line also improves. The minimum distance between the line and the circular patch depends on the fabrication precision and the materials used for the antenna.

Figure 6 demonstrates the S-parameter progression of the proposed structure. As it demonstrates, in all progression structures keep the S_{11} and S_{21} under −10 dB in the entire BW.

2.3 | Electric Fields

The current distributions corresponding to each excitation port are shown step-by-step in Figures 7 and 8. In these figures, Figure 7 illustrates the current distribution when Port A is excited and Port B is terminated with a matched load, where Figure 7a–e demonstrate the state of the E-field distribution of single patch at 0°, 45°, 90°, 135°, and 180°, respectively. Figure 8 presents the reverse case, with Port B excited and Port A matched, where Figure 8a–e demonstrate the state of the E-field distribution of single patch at 0°, 45°, 90°, 135° and 180°, respectively.

The rotation of the field in the patch, which is excited by coupling with the line, illustrates the rotation of the fields. Additionally, the electric field of rotation in Figure 7 is counter-clockwise and Figure 8 is clockwise.

Figure 9 demonstrates the electromagnetic field distribution from port A and port B. It reveals that the electromagnetic field distribution over the antenna is more intense at 12.5 GHz.

3 | Parametric Study

This section analyses the influence of key design parameters on the antenna's performance. Based on the insights gained from this analysis, the antenna structure was optimised to achieve the desired characteristics. Special emphasis was placed on compactness, as realising a space-efficient design was one of the primary objectives of this work. It is also important to note that during both simulation and measurement, the second port was terminated with a matched load to ensure accurate performance evaluation.

3.1 | Power Divider Parameters Analysis

In this section, the essential parameters of the power divider to understand their impact on the proposed structure are analysed.

The parameter W_t is the width of the essential line of the power divider studied from 4.2 to 5. Figures 10 and 11 illustrate the variation of simulated reflection and transmission coefficient (S_{11}) and (S_{21}) versus frequency for various W_t.

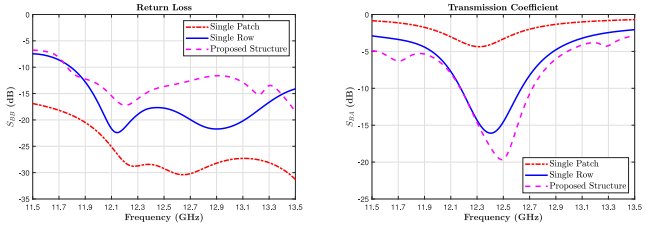

FIGURE 6 | Comparison of the proposed structure with the single patch and single row in terms of (a) return loss, and (b) transmission coefficient.

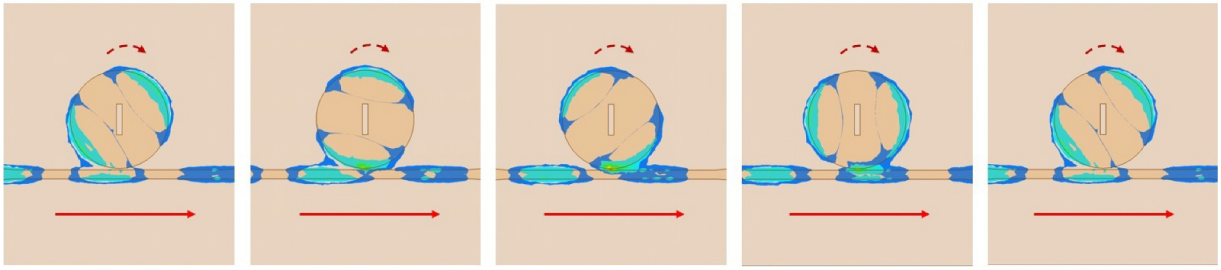

FIGURE 7 | The E-field distribution of single patch when port A is excited at (a) 0°, (b) 45°, (c) 90°, (d) 135°, and (e) 180°.

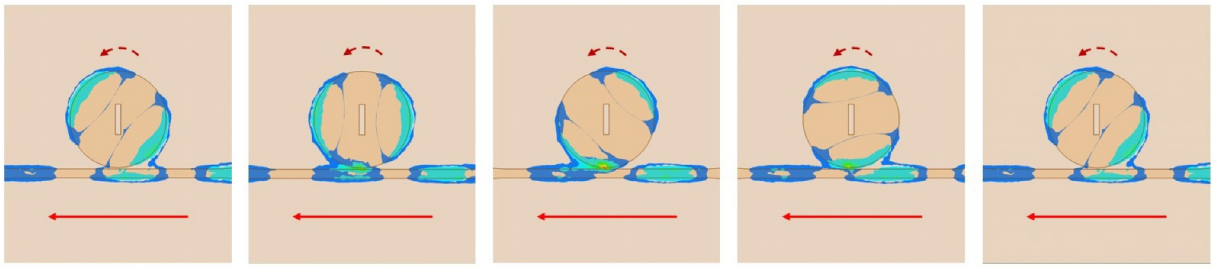

FIGURE 8 | The E-field distribution of single patch when port B is excited at (a) 0°, (b) 45°, (c) 90°, (d) 135°, and (e) 180°.

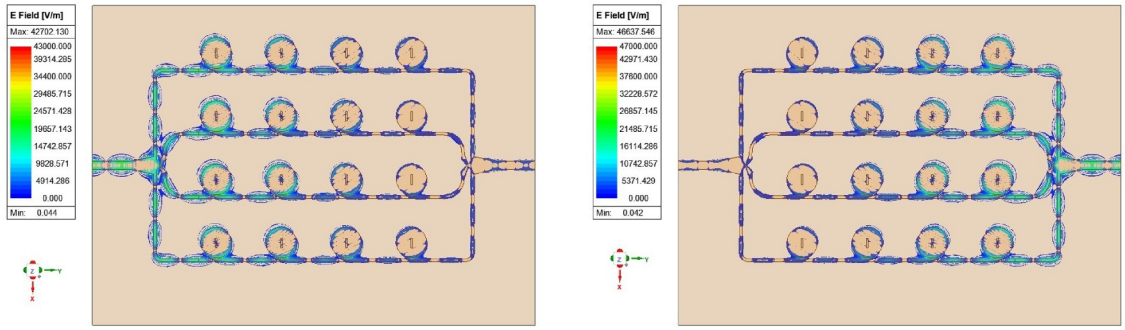

FIGURE 9 | The electric field distribution in the proposed antenna at the central frequency 12.45 GHz when (a) port A is excited, (b) port B is excited.

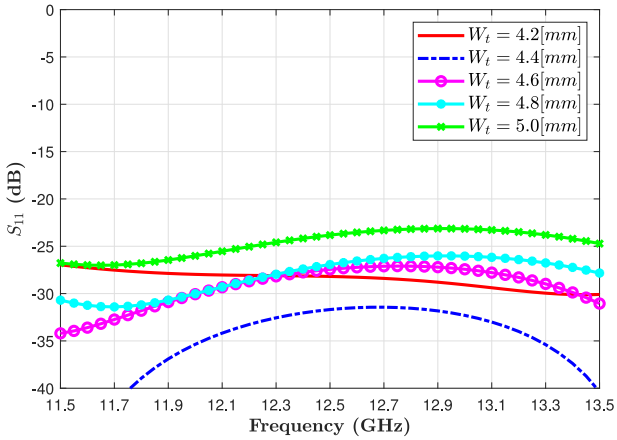

FIGURE 10 | The return loss (S_{11}) of the proposed power divider in the simulation results, when port A is excited by a load for various W_t.

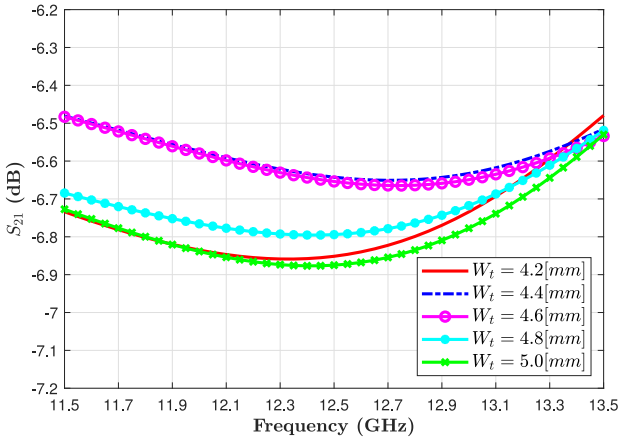

FIGURE 11 | The transmission coefficient (S_{21}) of the proposed power divider in the simulation results, when port A is excited by a load for various W_t.

As illustrated in Figure 10, an increase in W_t generally leads to a higher reflection coefficient of the power divider at the input port (S_{11}), whereas Figure 11 shows that under the same variation, the transmitted power tends to be reduced. Because these trends occur in an approximate rather than a strictly linear manner, $W_t = 4.6$ mm is selected as the optimal value to ensure overall structural efficiency.

The parameter L_t, which is the feed of the power divider, is analysed in Figures 12 and 13, where both demonstrate the trend of the S_{11} and S_{21} by variation of the L_t, respectively.

This parameter exhibits interesting sensitivity and can control the level of transmitted power, with greater length resulting in higher power transmission. However, reducing the size of all structures is an important consideration for wireless communication applications. As a result, it is critical to choose the appropriate dimension to reduce the dimension and also control the reflection and transmission coefficients.

The parameter T has an important role in defining the ratio of the power transmitted for the output ways of the power divider.

Figures 14 and 15 demonstrate the transmission coefficient of the internal and external branch ways by variation of the T. By increasing the T, the value of the S_{21} is raised because the external branch width is increased, and more power is transmitted by the external branch port on the other side; the value of S_{31} decreases because the width of the internal branch way is reduced. As a result, choosing this parameter correctly is vital for all efficiency performance structures.

The responses of $|S_{11}|$ and $|S_{21}|$ versus W_t and L_t are frequency-dependent and non-linear overall; we refer only to local monotonic behaviour near 12.45 GHz to guide the chosen values.

3.2 | Gap Between the Patch and Coupling Line *g* Variation Effect

Given the small g dimensions, the effects on the simulation results will be analysed. The impact of the gap between the coupling line and the circular patch (g) on the proposed antenna performance is studied by changing the g from 0.05 to 0.2 mm.

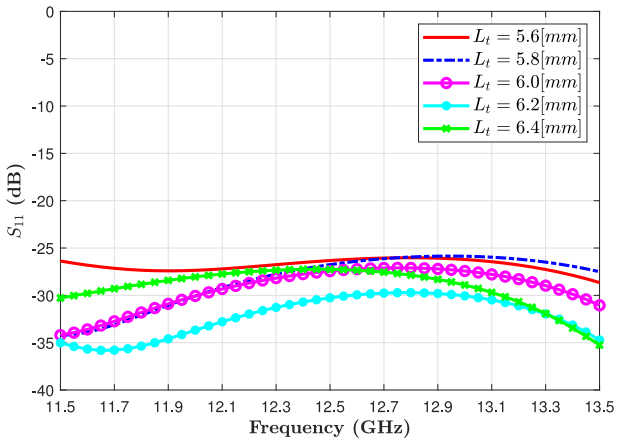

FIGURE 12 | The return loss (S_{11}) of the proposed power divider in the simulation results, when port A is excited by a load for various L_t.

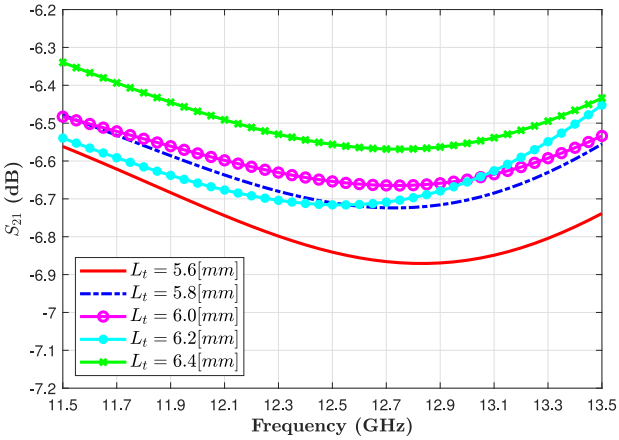

FIGURE 13 | The transmission coefficient (S_{21}) of the proposed power divider in the simulation results, when port A is excited by a load for various L_t.

Figure 16 illustrates the variation of simulated transmission coefficient (S_{AB}) versus frequency for various g.

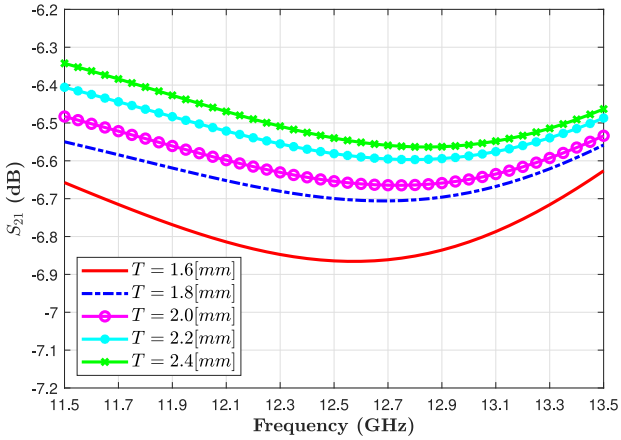

FIGURE 14 | The transmission coefficient of the internal branch way (S_{21}) of the proposed power divider in the simulation results, when port A is excited load for various T.

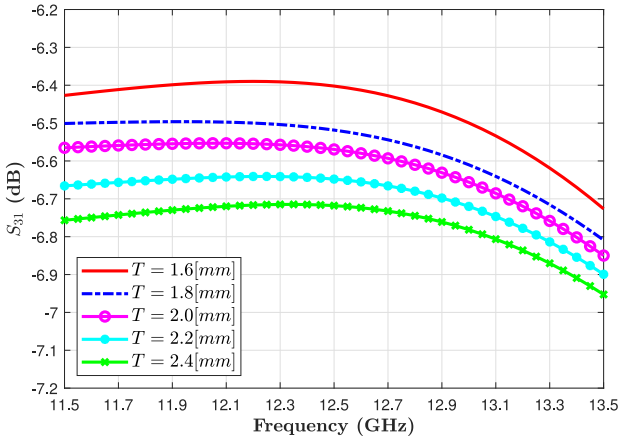

FIGURE 15 | The transmission coefficient of the external branch way (S_{31}) of the proposed power divider in the simulation results, when port A is excited load for various T.

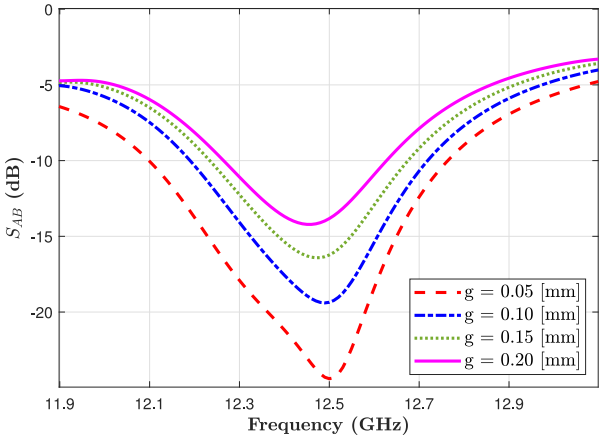

FIGURE 16 | S_{AB} of the proposed structure in the simulation results, when port B is excited, and port A is matched for various g.

In addition, the figure shows that decreasing the gap increases port isolation over the desired BW. The simulations confirm that the optimal gap value is $g = 0.1$ mm to achieve the desired broadband BW and good impedance matching.

As illustrated in Figure 16, the value of BW is increased by decreasing the size of g (when g is 0.05 mm, the BW improved). However, it is not economically feasible and not conventional due to the complexity of the fabrication process.

Similar to Figure 16, the value of the g is also varied to analyse the return loss (even though the prototype of the structure is symmetrical; in this section, port B is analysed), as depicted in Figure 17. By changing the g from 0.1 to 0.2 mm, the value of the return loss (S_{BB}) decreases at the central frequency. Moreover, it is shown that the optimal value of the g is the same as Figure 16, is $g = 0.1$ mm, for which the suggested antenna achieves the desired broadband BW with good impedance matching.

Figure 18 shows how the realised gain changes for various g. A small (≈ 1.7 dB) gain undulation is observed within 12.2–12.7 GHz. This is attributed to the frequency-dependent array factor of the series-fed branches together with residual input mismatch and inter-port coupling ($|S_{AA}|$ & $|S_{BB}|$ near −10 dB; $|S_{AB}|$ & $|S_{BA}| \lesssim -12$ dB), which create shallow standing-wave modulation of the delivered power; in addition, the divider's internal/external paths exhibit slight frequency-dependent transmission, subtly altering the per-row excitation.

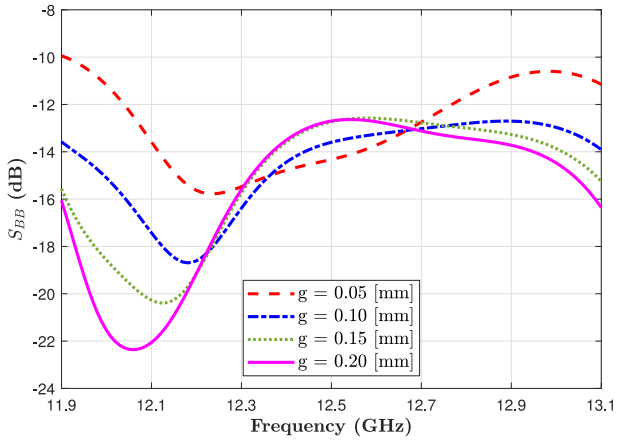

FIGURE 17 | S_{BB} of the proposed structure in the simulation results, when port B is excited and port A is matched for various g.

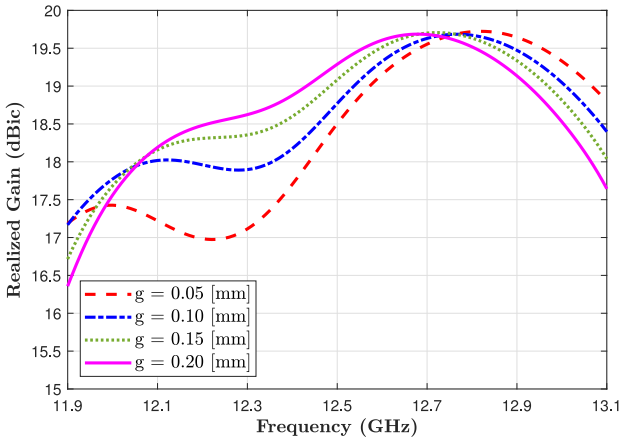

FIGURE 18 | LHCP realised gain of the proposed structure in the simulation results, when port B is excited and port A is matched for various g.

In Figure 18, as the g decreases, the realised gain decreases at the beginning of the frequency range. However, the g variation has no significant effect on the end of the desired operational frequency range. As a result, according to Figures 16–18, the appropriate value for g to have high BW and acceptable gain for wireless applications is 0.1 mm.

3.3 | Radius of the Circular Patch R_p Variation Effect

The parametric investigation in this section examines how the variation of the radius of the designed patch affects the realised gain on the resonant frequencies.

Figure 19 depicts the variation of realised gain when the R_p is changed, and all other dimensions remain constant. The figure shows that the parameter R_p has no crucial effect on the proposed antenna's value gain. However, the R_p changes the position of the maximum realised gain peak, which changes the resonant frequency. The range of this parameter (R_p) is between 4.2 and 4.4 mm. Moreover, the value of $R_p = 4.3$ mm provides an acceptable gain in the peak frequency at 12.5 GHz, which is 19.4 dBic.

4 | Measurement Results and Discussion

As shown in Figure 20a–c, a prototype of the proposed antenna has been fabricated and experimentally characterised to validate the structure's design.

According to the feeding design, if only one port is excited, the slotted circular patch array will generate an LHCP or an RHCP wave. Because of the similarity in values and forms, the

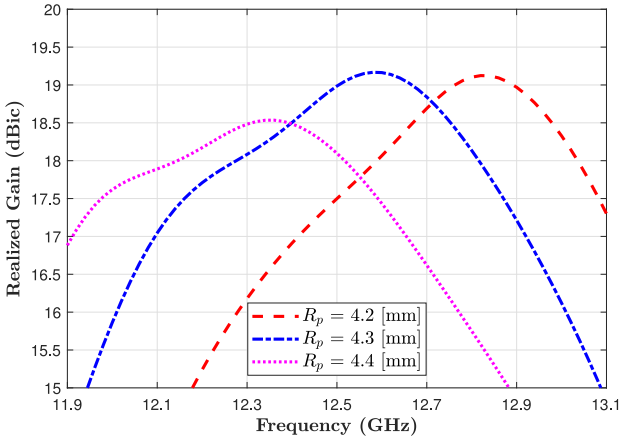

FIGURE 19 | LHCP realised gain of the proposed structure in the simulation results, when port B is excited and port A is matched for various R_p.

measurement results (AR, realised gain and radiation patterns) are only for the case where Port B (LHCP-Port) is excited. In the following, the simulation and measurement results will be compared.

4.1 | Reflection and Transmission Coefficient

As demonstrated in Figure 21, the antenna's simulated and measured reflection and transmission coefficients results demonstrate a good consistency. The operational BW of the antenna is characterised as the band where the measured reflection coefficients ($|S_{AA}|$ and $|S_{BB}|$) are below −10 dB. The transmission coefficients ($|S_{AB}|$ and $|S_{BA}|$) are below −12 dB.

In Figure 21, the operational BW of the proposed antenna is shown in the highlighted area.

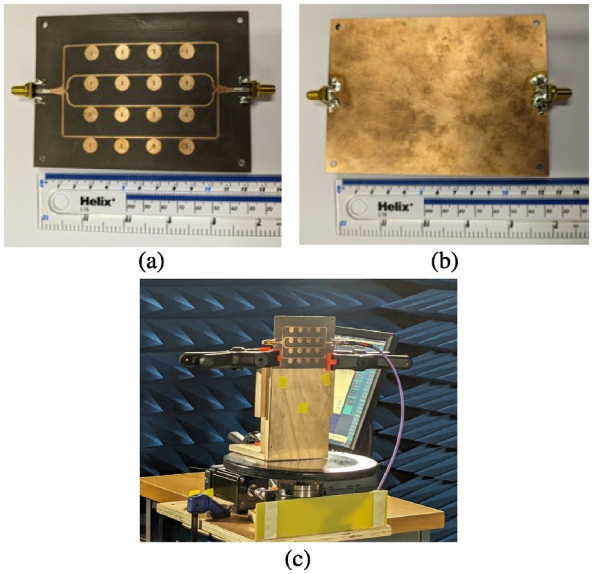

FIGURE 20 | Prototype of the proposed structure (a) top view, (b) bottom view, and (c) inside the anechoic chamber.

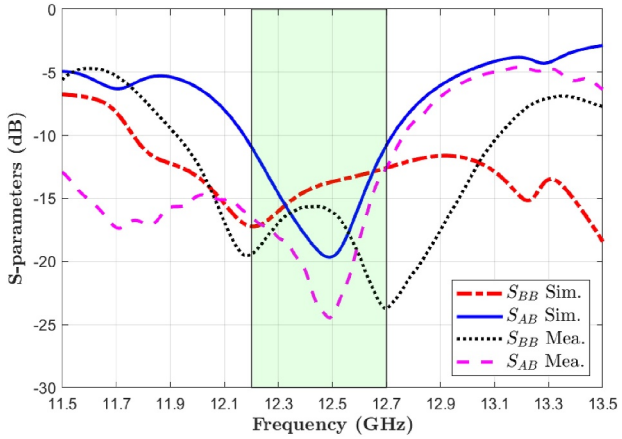

FIGURE 21 | Reflection and transmission coefficients of the proposed antenna.

4.2 | Axial Ratio

Figure 22 shows the simulated and measured AR values from 11.9 to 13.1 GHz. In this range, the simulated AR values are less than 2 dB. The AR values in the measurement results are less than 3 dB. Hence, the BW of the 3-dB AR is about 1.2 GHz. Moreover, the AR values at 12.45 GHz are 1.1 and 1.08 dB in measurement and simulation results, respectively.

4.3 | Realised Gain

Figure 23 illustrates the antenna's simulated and measured realised gain, and an acceptable agreement between the measurement and simulated results at all measured frequencies is achieved. For the measurement results, port B is excited and port A is matched by a 50 Ω broadband load.

By increasing the number of patches, the antenna array could achieve a higher gain; however, the number of sidelobes is increased. Without proper tapering, adding elements can increase sidelobe-level (SLL) due to uniform current distribution [63, 64].

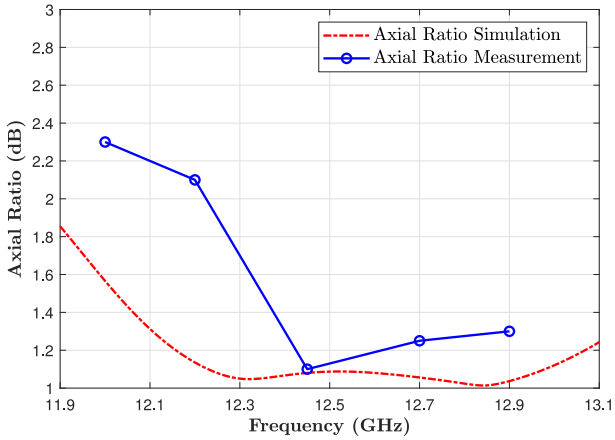

FIGURE 22 | AR of the proposed antenna, when port B is excited and port A is matched.

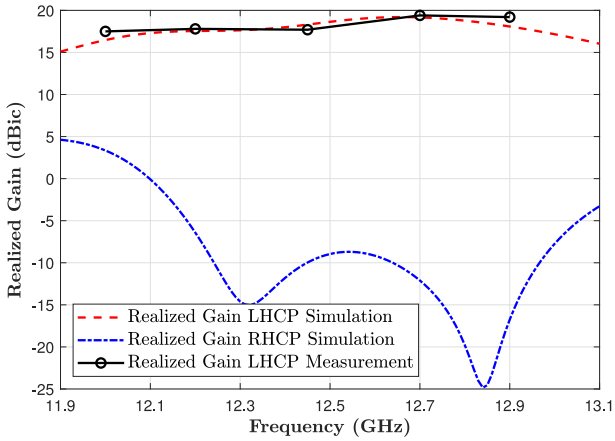

FIGURE 23 | Realized gain of the proposed antenna, when port B is excited and port A is matched.

As a result, to have a low-profile structure with acceptable gain while avoiding raising the sidelobe level, as demonstrated in Figure 1, four patches in each row are used.

The peak LHCP realised gain achieved in simulation and measurement results occurs at 12.7 GHz, equal to 19.4 dBic. In the operational frequency range, the RHCP realised gain is less than −6 dBic, whereas the LHCP and RHCP realised gains difference reported is at least 23 dB.

By employing the combination of high directivity, optimised radiating elements, efficient feed network and low losses in the antenna design, it is possible to focus the radiated energy in a specific direction, improving the antenna's overall gain.

4.4 | Radiation Patterns

In radiation pattern results, Port B (LHCP-Port) is excited in the measurement setup and a 50 Ω load matches Port A (RHCP-Port) to measure the radiation pattern. The measured and simulated 12.2, 12.45 and 12.7 GHz normalised radiation patterns in the antenna's *xz*- and *yz*- planes are shown in Figure 24. Satisfying consistency is achieved in the simulation and measurement results.

The measurements of LHCP show good agreement with the simulations across all three frequencies. However, the large RHCP discrepancy (up to ≈17 dB at boresight) between the simulated and measured results arises because RHCP is the cross-pol component when Port B (LHCP port) is excited; thus, we are comparing a very small quantity whose level is highly sensitive to measurement imperfections. In our setup, the main contributors are probe purity & dynamic range, pointing/alignment sensitivity and fabrication/substrate tolerances & feed termination.

Figure 24 presents the normalised radiation patterns in both the *xz*- and *yz*-planes at 12.2, 12.45 and 12.7 GHz, comparing simulated and measured results.

The radiation pattern results for the *xz*- and *yz*-planes at 12.2, 12.45 and 12.7 GHz are shown in Figure 24a–f, respectively.

The measurements show good agreement with the simulations across all three frequencies. Minor differences between the simulated and measured patterns are observed, which can be attributed to fabrication tolerances and variations in substrate parameters. Nonetheless, the overall consistency validates the design and confirms the antenna's directional radiation characteristics. The proposed 4 × 4 circularly polarised series-fed

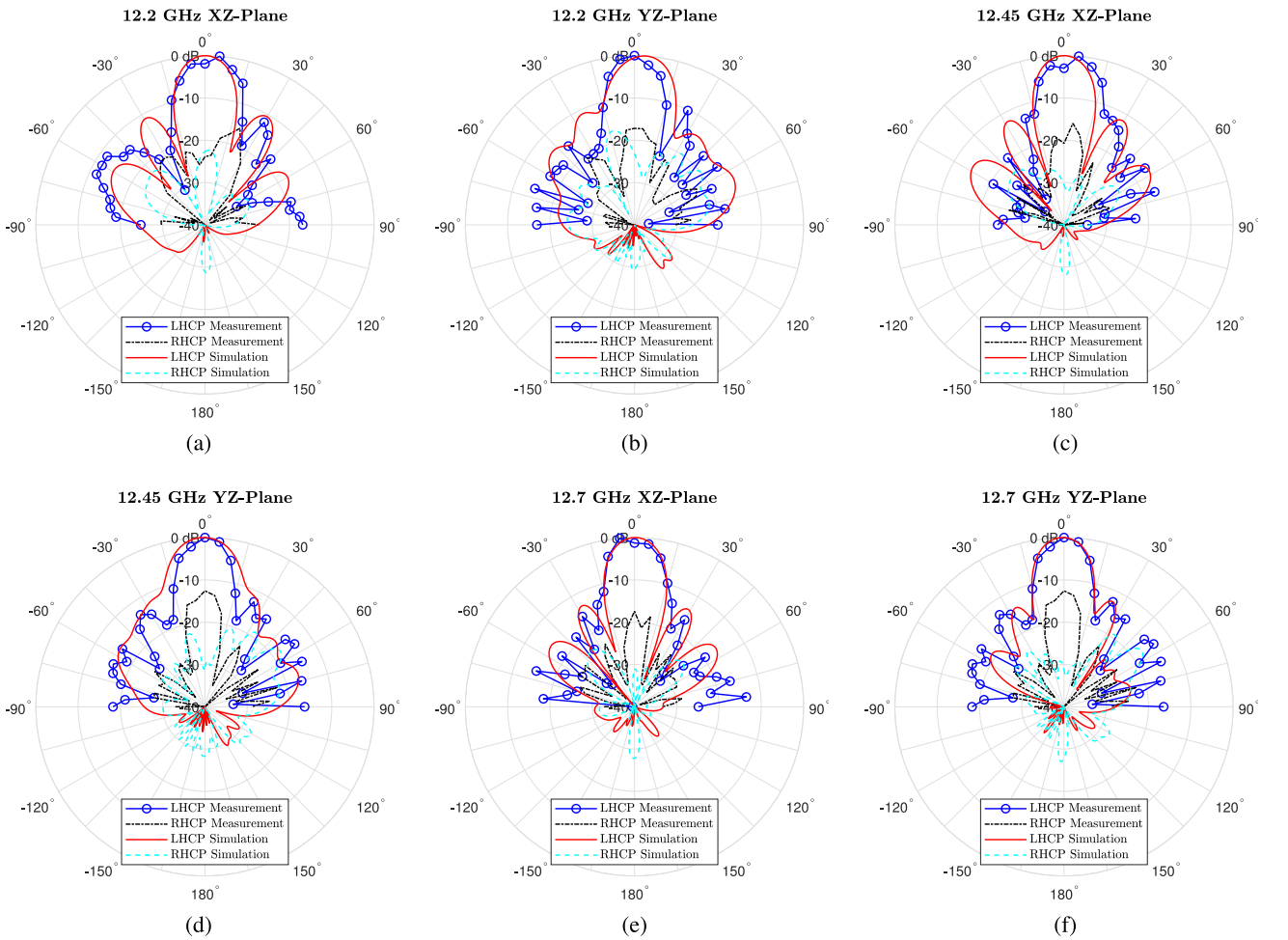

FIGURE 24 | Simulated and measured radiation patterns at three frequency samples: (a) at 12.2 GHz in *xz*-plane, (b) at 12.2 GHz in *yz*-plane, (c) at 12.45 GHz in *xz*-plane, (d) at 12.45 GHz in *yz*-plane, (e) at 12.7 GHz in *xz*-plane, and (f) at 12.7 GHz in *yz*-plane.

array exhibits a measured side-lobe level of approximately −13 dB to −15 dB, as observed in the radiation patterns shown in Figure 24. This level of SLL is acceptable for directional point-to-point communication applications. Increasing the number of elements per feed branch would enhance the antenna's peak gain by expanding the effective aperture, but could also raise the SLL if uniform excitation is used. This is because of increased constructive interference in side directions. Tapered feeding could be employed to mitigate this effect. Conversely, reducing the number of series-fed elements would naturally suppress side lobes and simplify the structure, but at the cost of lower peak gain and reduced beam directivity. In the proposed design, using four elements per branch was a deliberate choice to balance high gain (19.4 dBic), acceptable SLL and compact structure without requiring additional tapering.

5 | Discussion and Comparison

Table 1 provides a comparative analysis of the proposed antenna and several related works in terms of radiating elements, peak gain, polarisation type, total bandwidth (BW), physical size (in terms of free-space wavelength, λ_0), thickness, number of layers and central frequency.

The proposed antenna demonstrates a dual-circular polarisation (dual-CP) capability over the operating bandwidth with a high peak realised gain of 19.4 dBic, outperforming all other designs listed in the table that use a 4 × 4 array configuration. According to the axial ratio (AR) criterion, circular polarisation is assumed for AR values below 3 dB. An important advantage of the proposed antenna is its compact profile, achieved using a thinner substrate compared to other designs with similar radiating structures. Additionally, it uses only 4 × 4 slotted circular patches, yet achieves the highest effective gain per patch, approximately 7.4 dBic per element (19.4 dBic total gain divided by 4 × 4 effective radiating rows/columns), which indicates highly efficient radiation performance. A distinctive feature of the proposed structure is the integration of two separate compact power dividers, enabling selectable LHCP or RHCP operation with high gain and efficient bandwidth utilisation. This level of flexibility and performance in a relatively compact form factor makes the proposed antenna a strong candidate for modern wireless applications, including high-gain dual-CP systems. The achieved high-directivity of 19.4 dBic is primarily attributed to three key aspects of the design:

- The optimised 4 × 4 series-fed slotted circular patch array increases the effective aperture area.
- The compact single-stage 1-to-4 power divider minimises losses and maintains uniform amplitude and phase across the elements.
- The use of slot-loaded circular patches with coplanar proximity coupling improves polarisation purity and suppresses surface waves.

Although not explicitly reported, the antenna shows strong indications of high aperture efficiency, as its gain is well-aligned with its physical aperture. Additionally, the close match between simulated and measured realised gain suggests high radiation efficiency, thanks to low-loss materials, minimal feed losses and optimised coupling. These combined factors contribute to the antenna's ability to deliver high gain while maintaining compactness and efficiency.

It is notable to note that the proposed structure has an interesting advantage that by employing two distinguished power dividers can generate dual-CP with high gain and appropriate bandwidth. Therefore, the proposed antenna is a good candidate for wireless applications.

Aperture efficiency provides a more meaningful figure of merit than gain alone. It quantifies how effectively an antenna converts its physical area into radiated power and is defined by Ref. [54] as follows:

$$e_a = \frac{G}{4\pi \text{in} A_{\text{phy}} \lambda^2} \tag{5}$$

where G is the maximum gain of the antenna and A_{phy} is the physical aperture (size) of the antenna. At the centre frequency

TABLE 1 | Comparison between the proposed antenna and related works.

Antenna structure	Radiating elements	Peak gain (dBi/dBic)	Polarisation type	Total BW(%)	Size ($\lambda_0 \times \lambda_0$)	Thickness (λ_0)	No. of layers	Central freq. (GHz)	Aperture eff. e_a(%)
[32]	4 × 4	12	LHCP	2.45	3.48 × 3.48	0.035	1	8.15	10.41
[54]	4 × 4	14.6	Dual-CP	4.18	4.30 × 4.32	0.021	1	11.9	12.35
[65]	4 × 4	17.1	Linear	19.35	2.49 × 2.29	0.161	3	12.0	71.57
[66]	2 × 2	11.04	Linear	1.01	1.41 × 1.41	0.049	2	5.82	50.85
[67]	8 × 18	27.3	Dual-CP	3.87	5.41 × 24.21	—	1	77.5	3.26
[68]	2 × 2	10.91	Dual-CP	1.45	1.93 × 1.93	0.051	1	9.65	22.32
[69]	4 × 4	16.65	RHCP	8.53	2.52 × 2.52	0.043	1	8.25	57.94
[70]	1 × 20	10.0	LHCP	4.1	5.07 × 0.29	0.020	1	9.75	54.12
[71]	1 × 4	12.8	Linear	4.1	2.70 × 0.90	0.070	1	27	62.40
[72]	4 × 4	15.8	RHCP	22.2	2.25 × 2.25	0.141	3	13.0	59.76
This work	4 × 4	19.4	Dual-CP	4.0	5.19 × 3.73	0.033	1	12.45	36.73

of 12.45, the proposed arrays demonstrate aperture efficiencies of 36.73%.

This work, compared to the other works presented in Table 1, offers a higher gain and aperture efficiency with dual-CP. By layering the structure and adding a director layer, the antenna aperture efficiency is increased [72].

6 | Conclusion

This research presents the development of a novel high-gain low-profile 4 × 4 microstrip patch array antenna with dual-CP capabilities.

The key innovation lies in the integration of two compact and symmetrical 1-to-4 microstrip power divider networks, enabling the antenna to operate in either left-hand circular polarisation (LHCP) or right-hand circular polarisation (RHCP) modes by selectively exciting the corresponding input port. Unlike many conventional dual-CP antennas that require multilayer or complex configurations, the proposed design achieves dual-CP functionality in a single-layer planar structure—greatly simplifying fabrication while maintaining high performance.

The antenna effectively addresses several important challenges, including compactness, gain, bandwidth and port isolation. It achieves a peak realised gain of 19.4 dBic and operates across a 500 MHz bandwidth with an axial ratio below 3 dB. These performance metrics represent a significant improvement compared to other reported 4 × 4 patch array designs. Additionally, the use of proximity-coupled slotted circular patches enhances polarisation purity and radiation efficiency, contributing to consistent performance across the operating band.

From a practical standpoint, the antenna features a simple layout, uses a thin substrate and supports low-cost fabrication, making it well-suited for integration into modern wireless systems. Its combination of high gain, compact form and dual-CP functionality makes it a strong candidate for a wide range of applications, including point-to-point communication, satellite systems, automotive radar and emerging 5G/6G technologies. Measurement results are in close agreement with simulations, confirming the reliability, efficiency and real-world applicability of the proposed design. Overall, this antenna offers an effective and versatile solution for future wireless communication systems requiring robust and flexible polarisation performance.

For future works, by adding a groove gap waveguide feeding network behind the proposed patch antenna array structure and also introducing a suitable director layer above the structure, higher gain and efficiency could be achieved.

Author Contributions

Mahdi Parvaneh: conceptualization, data curation, formal analysis, investigation, methodology, resources, software, validation, writing –original draft. **Hassan Zakeri:** conceptualization, data curation, formal analysis, methodology, resources, software, validation, writing – original draft. **Gholamreza Moradi:** conceptualization, data curation, formal analysis, investigation, project administration, supervision, validation, writing – review and editing. **Mohammad Alibakhshikenari:** conceptualization, formal analysis, funding acquisition, investigation, methodology, project administration, resources, supervision, validation, visualization, writing – review and editing. **Bandar Alshammari:** data curation, resources, validation, writing – review and editing. **Chan Hwang See:** conceptualization, data curation, methodology, resources, validation, writing – review and editing. **Bal Virdee:** conceptualization, methodology, investigation, writing – review and editing. **Symon K. Podilchak:** data curation, formal analysis, investigation, resources, validation, writing – review and editing. **Ernesto Limiti:** conceptualization, methodology, investigation, writing – review and editing.

Acknowledgements

Co-funded by the European Union. Views and opinions expressed are, however, those of the author(s) only and do not necessarily reflect those of the European Union or the European Research Executive Agency. Neither the European Union nor the granting authority can be held responsible for them. Besides that, this publication has emanated from research jointly funded by Taighde Éireann—Research Ireland under (Grant 13/RC/2094-2), the European Union's Marie Sklodowska-Curie Actions under (Grant 101126578), and was supported in part by the University of Galway.

Conflicts of Interest

The authors declare no conflicts of interest.

Data Availability Statement

The data that support the findings of this study are available from the corresponding author upon reasonable request.

References

1. D. Zarifi, A. Farahbakhsh, and A. U. Zaman, "Design of a Dual-CP Gap Waveguide Fed Aperture Array Antenna," *IET Microwaves, Antennas & Propagation* 17, no. 9 (2023): 723–730, https://doi.org/10.1049/mia2.12379.

2. Y. Luo, Z. Chen, Z. Hu, and C. Li, "Wideband Circularly Polarised Antenna With Dual-Fed Strategy Simplification Based on Common Mode and Differential Mode," *IET Microwaves, Antennas & Propagation* 17, no. 11 (2023): 840–845, https://doi.org/10.1049/mia2.12400.

3. D. Jing, H. Li, X. Ding, W. Shao, and S. Xiao, "Compact and Broadband Circularly Polarized Implantable Antenna for Wireless Implantable Medical Devices," *IEEE Antennas and Wireless Propagation Letters* 22, no. 6 (2023): 1236–1240, https://doi.org/10.1109/lawp.2023.3237558.

4. M. Moharana and B. Dwivedy, "Circularly Polarized Planar Antennas With Enhanced Characteristics for Contemporary Wireless Communication Use Cases: A Review," *IEEE Access* 12 (2024): 134594–134613, https://doi.org/10.1109/access.2024.3415483.

5. Y. Zhang, C. Liu, X. Liu, and K. Zhang, "A Miniaturized Circularly Polarized Implantable RFID Antenna for Biomedical Applications," *International Journal of RF and Microwave Computer-Aided Engineering* 30, no. 3 (2020): e22105, https://doi.org/10.1002/mmce.22105.

6. H. Q. Nguyen and M. T. Le, "Multiband Ambient Rf Energy Harvester With High Gain Wideband Circularly Polarized Antenna Toward Self-Powered Wireless Sensors," *Sensors* 21, no. 21 (2021): 7411, https://doi.org/10.3390/s21217411.

7. P. Khoddami, H. Zakeri, G. Moradi, et al., "Thz Antenna Assisted by Graphene for 6G Communications," in *2024 17th United Conference on Millemetre Waves and Terahertz Technologies (UCMMT)* (IEEE, 2024), 151–155.

8. D. Warmowska, K. A. Abdalmalak, L. E. G. Muñoz, and Z. Raida, "High-Gain, Circularly-Polarized Thz Antenna With Proper Modeling of Structures With Thin Metallic Walls," *IEEE Access* 8 (2020): 125223–125233, https://doi.org/10.1109/access.2020.3007576.

9. R. Azizpour, H. Zakeri, G. Moradi, et al., "Multi-Channel Radio-Over-fiber Communication Systems Through Modulation Instability Phenomenon," *IEEE Photonics Journal* 16, no. 5 (2024): 1–13, https://doi.org/10.1109/jphot.2024.3446314.

10. A. Sabban, "Wearable Circular Polarized Antennas for Health Care, 5G, Energy Harvesting, and Iot Systems," *Electronics* 11, no. 3 (2022): 427, https://doi.org/10.3390/electronics11030427.

11. L. H. Trinh, N. V. Truong, and F. Ferrero, "Low Cost Circularly Polarized Antenna for Iot Space Applications," *Electronics* 9, no. 10 (2020): 1564, https://doi.org/10.3390/electronics9101564.

12. S. A. Khorasani, H. Zakeri, G. Moradi, M. Alibakhshikenari, C. H. See, and E. Limiti, "Orbital Angular Momentum With the Approach of Using in Sub-6ghz 5g Mobile Communications for Wireless Applications," in *2024 6th Global Power, Energy and Communication Conference (GPECOM)* (IEEE, 2024), 1–4.

13. N. Hussain, T. D. Pham, and H.-H. Tran, "Circularly Polarized Mimo Antenna With Wideband and High Isolation Characteristics for c-Band Communication Systems," *Micromachines* 13, no. 11 (2022): 1894, https://doi.org/10.3390/mi13111894.

14. H. Zakeri, R. Azizpour, P. Khoddami, et al., "Low-Cost Multiband Four-Port Phased Array Antenna for Sub-6 Ghz 5g Applications With Enhanced Gain Methodology in Radio-Over-Fiber Systems Using Modulation Instability," *IEEE Access* 12 (2024): 117787–117799, https://doi.org/10.1109/access.2024.3446313.

15. Z. M. Phyo, T. Fujimoto, and C.-E. Gaun, "A Circularly Polarised Multiple Input Multiple Output Antenna With Single-Sense for Sub-6 Ghz 5g Applications," *IET Microwaves, Antennas & Propagation* 17, no. 14 (2023): 1082–1092, https://doi.org/10.1049/mia2.12426.

16. H. Zakeri, P. Khoddami, G. Moradi, et al., "Path Loss Model Estimation at Indoor Offices Environment by Using Deep Neural Network and Catboost for Millimeter Wave 5g Wireless Application," *IEEE Access* (2024), https://doi.org/10.1109/ACCESS.2024.3487118.

17. Z. Zhao, F. Liu, J. Ren, Y. Liu, and Y. Yin, "Dual-Sense Circularly Polarized Antenna With a Dual-Coupled Line," *IEEE Antennas and Wireless Propagation Letters* 19, no. 8 (2020): 1415–1419, https://doi.org/10.1109/lawp.2020.3003943.

18. J. Kulkarni, B. Garner, Y. Li, et al., "A Dual-CP Quad-Port Mimo Antenna With Reduced Mutual Coupling for x-Band Application," *IEEE Antennas and Wireless Propagation Letters* 22, no. 9 (2023): 2085–2089, https://doi.org/10.1109/lawp.2023.3275530.

19. C. Murat, M. Alibakhshikenari, P. Parand, et al., "Millimeter-Wave Antenna Design Inspired by Half-Ring Resonators for 5g Communication Systems," in *2024 2nd International Conference on Information Network and Computer Communications (INCC)* (IEEE, 2024), 59–64.

20. P. Squadrito, S. Zhang, and G. F. Pedersen, "X-Band Dual Circularly Polarized Patch Antenna With High Gain for Small Satellites," *IEEE Access* 7 (2019): 74925–74930, https://doi.org/10.1109/access.2019.2921088.

21. M. El Hammoumi, N. E. A. El Idrissi, R. Raad, P. I. Theoharis, F. Tubbal, and S. Abulgasem, "Ultra Wideband Dual Circularly Polarized Patch Antenna for 5g and Cubesat Applications," in *2022 9th International Conference on Wireless Networks and Mobile Communications (WINCOM)* (IEEE, 2022), 1–6.

22. H. Zakeri, R. S. Shirazi, and G. Moradi, "An Accurate Model to Estimate 5g Propagation Path Loss for the Indoor Environment," preprint arXiv:2302.10057 (2023).

23. J. Iqbal, U. Illahi, M. A. Khan, et al., "A Novel Single-Fed Dual-Band Dual-Circularly Polarized Dielectric Resonator Antenna for 5g Sub-6ghz Applications," *Applied Sciences* 12, no. 10 (2022): 5222, https://doi.org/10.3390/app12105222.

24. H. Nawaz, A. U. Niazi, and M. Ahmad, "Dual Circularly Polarized Patch Antenna With Improved Interport Isolation for s-Band Satellite Communication," *International Journal of Antennas and Propagation* 2021 (2021): 1–10, https://doi.org/10.1155/2021/8022207.

25. S. Chaudhuri, M. Mishra, R. S. Kshetrimayum, R. K. Sonkar, S. Bhattacharjee, and B. Saha, "High Port-to-Port Isolation Dual Circularly Polarised Microstrip Patch Antenna With Multifunction Dgs," *IET Microwaves, Antennas & Propagation* 14, no. 15 (2020): 2035–2044, https://doi.org/10.1049/iet-map.2020.0094.

26. A. Thakur, A. Sharma, and I. J. G. Zuazola, "A Wearable Circulator-Like Circularly Polarised Antenna for Full-Duplex Wireless Body Area Network Applications," *IET Microwaves, Antennas & Propagation* 18, no. 11 (2024): 838–848, https://doi.org/10.1049/mia2.12507.

27. Y.-H. Yang, B.-H. Sun, and J.-L. Guo, "A Low-Cost, Single-Layer, Dual Circularly Polarized Antenna for Millimeter-Wave Applications," *IEEE Antennas and Wireless Propagation Letters* 18, no. 4 (2019): 651–655, https://doi.org/10.1109/lawp.2019.2900301.

28. J. Liu, J.-Y. Li, R. Xu, et al., "A Wideband Double Circularly Polarized Slot Antenna With Unidirectional Patterns," in *2018 IEEE International Symposium on Antennas and Propagation & USNC/URSI National Radio Science Meeting* (IEEE, 2018), 1283–1284.

29. H. Zakeri, M. Veysi, G. Moradi, et al., "A Compact Dual Circularly Polarized Mimo Antenna With Controlled Slots for 5g Wireless Applications Across mm-Wave Spectrum," in *2024 17th United Conference on Millemetre Waves and Terahertz Technologies (UCMMT)* (IEEE, 2024), 194–198.

30. S. J. Chen, C. Fumeaux, Y. Monnai, and W. Withayachumnankul, "Dual Circularly Polarized Series-Fed Microstrip Patch Array With Coplanar Proximity Coupling," *IEEE Antennas and Wireless Propagation Letters* 16 (2017): 1500–1503, https://doi.org/10.1109/lawp.2016.2647227.

31. D. Swathi, H. Khan, V. Pallavi, S. Shalini, and K. Pratyusha, "Design and Implementation of Dual Feed Circularly Polarized Dielectric Resonator Antenna for High Gain Applications," in *2020 International Conference on Inventive Computation Technologies (ICICT)* (IEEE, 2020), 907–911.

32. M. Elahi, S. Trinh-Van, Y. Yang, K.-Y. Lee, and K.-C. Hwang, "Compact and High Gain Circularly Polarized Microstrip Patch Antenna Array for Next Generation Small Satellite," *Applied Sciences* 11, no. 19 (2021): 8869, https://doi.org/10.3390/app11198869.

33. S. X. Ta and I. Park, "Compact Wideband Circularly Polarized Patch Antenna Array Using Metasurface," *IEEE Antennas and Wireless Propagation Letters* 16 (2017): 1932–1936, https://doi.org/10.1109/lawp.2017.2689161.

34. P. Pradeep, S. Satyanarayana, and M. Mahesh, "Design and Analysis of a Circularly Polarized Omnidirectional Slotted Patch Antenna at 2.4 Ghz," *ICTACT Journal on communication technology* 11, no. 3 (2020): 2234–2238, https://doi.org/10.21917/ijct.2020.0330.

35. D. K. Barik, K. Mondal, and M. Azharuddin, "Broad Axial Ratio Bandwidth Circularly Polarized With Wide Angle Coverage Planar Monopole Antenna," *AEU-International Journal of Electronics and Communications* 164 (2023): 154627, https://doi.org/10.1016/j.aeue.2023.154627.

36. M. A. Hossain, M. A. Rahman, A. H. Murshed, E. Nishiyama, and I. Toyoda, "A Simple Design and Fabrication of Polarization Reconfigurable Antenna for Industrial Scientific and Medical-Band Applications," *International Journal of Electrical and Computer Engineering* 13, no. 2 (2023): 1580, https://doi.org/10.11591/ijece.v13i2.pp1580-1587.

37. X. Teng, Y. Hou, S. Wang, and K. Ma, "Low-Profile High-Gain Circularly Polarized Endfire Leaky-Wave Antenna," *IEEE Transactions*

on Antennas and Propagation 72, no. 10 (2024): 8046–8051, https://doi.org/10.1109/tap.2024.3452005.

38. N. Hussain, M.-J. Jeong, J. Park, and N. Kim, "A Broadband Circularly Polarized Fabry-Perot Resonant Antenna Using a Single-Layered Prs for 5g Mimo Applications," *IEEE Access* 7 (2019): 42897–42907, https://doi.org/10.1109/access.2019.2908441.

39. M. S. Ibrahim, H. Attia, Q. Cheng, and A. Mahmoud, "Wideband Circularly Polarized Aperture Coupled Dra Array With Sequential-Phase Feed at x-Band," *Alexandria Engineering Journal* 59, no. 6 (2020): 4901–4908, https://doi.org/10.1016/j.aej.2020.09.005.

40. R. Kumari, R. K. Gangwar, and R. K. Chaudhary, "Investigation on Rotated Rectangular Slots to Improve the Circular Polarization in Cylindrical Dielectric Resonator Antenna," *IEEE Access* 9 (2021): 97327–97336, https://doi.org/10.1109/access.2021.3093898.

41. Z. Xiao, Y. Cao, W. Che, and Q. Xue, "Millimeter-Wave Filtering Circularly Polarized Antenna Using Hybrid Radiation Modes for Satellite Applications," *IEEE Transactions on Antennas and Propagation* 72, no. 10 (2024): 7584–7593, https://doi.org/10.1109/tap.2024.3447787.

42. W. Yang, J. Li, D. Chen, Y. Cao, Q. Xue, and W. Che, "Advanced Metasurface-Based Antennas: A Review," *IEEE Open Journal of Antennas and Propagation* 6, no. 1 (2024): 6–24, https://doi.org/10.1109/ojap.2024.3465513.

43. I. Nadeem and D.-Y. Choi, "Study on Mutual Coupling Reduction Technique for Mimo Antennas," *IEEE Access* 7 (2018): 563–586, https://doi.org/10.1109/access.2018.2885558.

44. S. Soltani and R. D. Murch, "A Compact Planar Printed Mimo Antenna Design," *IEEE Transactions on Antennas and Propagation* 63, no. 3 (2015): 1140–1149, https://doi.org/10.1109/tap.2015.2389242.

45. Y. M. Pan, Y. Hu, and S. Y. Zheng, "Design of Low Mutual Coupling Dielectric Resonator Antennas Without Using Extra Decoupling Element," *IEEE Transactions on Antennas and Propagation* 69, no. 11 (2021): 7377–7385, https://doi.org/10.1109/tap.2021.3090807.

46. S. Kim and S. Nam, "A Compact and Wideband Linear Array Antenna With Low Mutual Coupling," *IEEE Transactions on Antennas and Propagation* 67, no. 8 (2019): 5695–5699, https://doi.org/10.1109/tap.2019.2922833.

47. R. Selvaraju, M. H. Jamaluddin, M. R. Kamarudin, J. Nasir, and M. H. Dahri, "Mutual Coupling Reduction and Pattern Error Correction in a 5g Beamforming Linear Array Using Csrr," *IEEE Access* 6 (2018): 65922–65934, https://doi.org/10.1109/access.2018.2873062.

48. L. Han, H. Yin, M. Gao, and J. Xie, "A Superdirective Beamforming Approach With Impedance Coupling and Field Coupling for Compact Antenna Arrays," *IEEE Open Journal of the Communications Society* 5 (2024): 7262–7277, https://doi.org/10.1109/ojcoms.2024.3497985.

49. M. Salarrahimi, V. Volski, and G. A. Vandenbosch, "Mutual Coupling-Based Compact Wideband Circularly Polarized Antenna," *IEEE Transactions on Antennas and Propagation* 67, no. 7 (2019): 4872–4877, https://doi.org/10.1109/tap.2019.2916679.

50. Y. Chen and D. Manteuffel, "A Tunable Decoupling and Matching Concept for Compact Mobile Terminal Antennas," *IEEE Transactions on Antennas and Propagation* 65, no. 4 (2017): 1570–1578, https://doi.org/10.1109/tap.2017.2670318.

51. M. O. Bagheri, H. R. Hassani, and A. R. Sebak, "Stable Phase-Centre Horn Antenna Using 3d Printed Dielectric Rod for Aperture Efficiency Improvement of Space-Fed Antennas," *IET Microwaves, Antennas & Propagation* 16, no. 14 (2022): 888–897, https://doi.org/10.1049/mia2.12303.

52. R. Azizpour, H. Zakeri, and G. Moradi, "Beam Pattern Control for Graphene-Based Patch Array Antenna With Radio-Over-Fiber Systems by Using Modulation Instability Phenomenon," *Optics Continuum* 2, no. 4 (2023): 865–876, https://doi.org/10.1364/optcon.480231.

53. Y. S. Yong, A. L. Low, S. F. Chien, A. H. You, H.-Y. Wong, and Y. K. Chan, "Design and Analysis of Equal Power Divider Using 4-Branch Waveguide," *IEEE Journal of Quantum Electronics* 41, no. 9 (2005): 1181–1187, https://doi.org/10.1109/jqe.2005.852990.

54. H. Zakeri, M. Parvaneh, and G. Moradi, "A Compact Rhcp and Lhcp Truncated Corner Patch Series-Fed Array Antenna," *International Journal of Electronics Letters* 11, no. 1 (2023): 125–133, https://doi.org/10.1080/21681724.2022.2062789.

55. E. Al Abbas, A. Abbosh, and K. Bialkowski, "Tunable In-Phase Power Divider for 5g Cellular Networks," *IEEE Microwave and Wireless Components Letters* 27, no. 6 (2017): 551–553, https://doi.org/10.1109/lmwc.2017.2701307.

56. L. Liu, L. Zhu, Z.-B. Wang, and Y.-R. Zhang, "Proposal and Synthesis of Self-Packaged Wideband Bandpass Power Divider With Constant Power Ratio and Full Phase Difference Range," *IEEE Transactions on Microwave Theory and Techniques* 73, no. 3 (2024): 1645–1658, https://doi.org/10.1109/tmtt.2024.3452313.

57. S. Hu, K. Song, F. Zhang, Y. Zhu, and Y. Fan, "A Novel Compact Wideband Four-Way w-Band Waveguide Power Divider With Low Insertion Loss," in *2016 IEEE MTT-S International Microwave Workshop Series on Advanced Materials and Processes for RF and Thz Applications (IMWS-AMP)* (IEEE, 2016), 1–3.

58. S. Park and S. Hong, "Millimeter-Wave Wideband Differential Four-Way Wilkinson Power Divider With 90 Rotational Symmetric Layout," *IEEE Microwave and Wireless Components Letters* 32, no. 10 (2022): 1163–1166, https://doi.org/10.1109/lmwc.2022.3172398.

59. G. Lee, S. Cho, and S. Hong, "A ka-Band Small-Size Differential Four-Way Wilkinson Power Divider With Multicoupled Inductors," *IEEE Microwave and Wireless Technology Letters* 34, no. 9 (2024): 1067–1070, https://doi.org/10.1109/lmwt.2024.3426618.

60. F.-J. Chen, L.-S. Wu, L.-F. Qiu, and J.-F. Mao, "A Four-Way Microstrip Filtering Power Divider With Frequency-Dependent Couplings," *IEEE Transactions on Microwave Theory and Techniques* 63, no. 10 (2015): 3494–3504, https://doi.org/10.1109/tmtt.2015.2457426.

61. H. Lin, Q. Chen, Y. Ji, X. Yang, J. Wang, and L. Ge, "Weak-Field-Based Self-Decoupling Patch Antennas," *IEEE Transactions on Antennas and Propagation* 68, no. 6 (2020): 4208–4217, https://doi.org/10.1109/tap.2020.2970109.

62. A. Y. Ashyap, S. H. B. Dahlan, Z. Z. Abidin, et al., "An Overview of Electromagnetic Band-Gap Integrated Wearable Antennas," *IEEE Access* 8 (2020): 7641–7658, https://doi.org/10.1109/access.2020.2963997.

63. D. H. Nguyen, J. Ala-Laurinaho, J. Moll, V. Krozer, and G. Zimmer, "Improved Sidelobe-Suppression Microstrip Patch Antenna Array by Uniform Feeding Networks," *IEEE Transactions on Antennas and Propagation* 68, no. 11 (2020): 7339–7347, https://doi.org/10.1109/tap.2020.2995416.

64. H. A. Diawuo, S. J. Lee, and Y.-B. Jung, "Sidelobe-Level Reduction of a Linear Array Using Two Amplitude Tapering Techniques," *IET Microwaves, Antennas & Propagation* 11, no. 10 (2017): 1432–1437, https://doi.org/10.1049/iet-map.2016.0883.

65. F. Karami, P. Rezaei, A. Amn-e Elahi, A. Abolfathi, and A. A. Kishk, "Broadband and Efficient Patch Array Antenna Fed by Substrate Integrated Waveguide Feed Network for ku-Band Satellite Applications," *International Journal of RF and Microwave Computer-Aided Engineering* 31, no. 9 (2021): e22772, https://doi.org/10.1002/mmce.22772.

66. J.-H. Ou, J. Huang, J. Liu, J. Tang, and X. Y. Zhang, "High-Gain Circular Patch Antenna and Array With Introduction of Multiple Shorting Pins," *IEEE Transactions on Antennas and Propagation* 68, no. 9 (2020): 6506–6515, https://doi.org/10.1109/tap.2020.2983793.

67. Z. Zang, A. U. Zaman, and J. Yang, "Single-Layer Dual-Circularly Polarized Series-Fed Gap Waveguide-Based Slot Array for a 77 Ghz Automotive Radar," *IEEE Transactions on Antennas and Propagation* 71, no. 5 (2023): 3775–3784, https://doi.org/10.1109/tap.2023.3243996.

68. V. K. Kothapudi and V. Kumar, "Compact and Dual Polarized Series-Fed Antenna Array for x-Band Airborne Synthetic Aperture Radar Applications," *Journal of electromagnetic engineering and science* 18, no. 2 (2018): 117–128, https://doi.org/10.26866/jees.2018.18.2.117.

69. D. Hester, S. Han, and M. Adams, "Design Methodology for Single-Feed Circularly Polarized x-Band Antenna Arrays for Cubesats Using Multilevel Sequential Rotation," *IEEE Journal on Miniaturization for Air and Space Systems* 5, no. 1 (2023): 42–50, https://doi.org/10.1109/jmass.2023.3333833.

70. S. Ogurtsov and S. Koziel, "A Conformal Circularly Polarized Series-Fed Microstrip Antenna Array Design," *IEEE Transactions on Antennas and Propagation* 68, no. 2 (2019): 873–881, https://doi.org/10.1109/tap.2019.2943326.

71. Y. Q. Guo, Y. M. Pan, and S. Y. Zheng, "Design of Series-Fed, single-layer, and Wideband Millimeter-Wave Microstrip Arrays," *IEEE Transactions on Antennas and Propagation* 68, no. 10 (2020): 7017–7026, https://doi.org/10.1109/tap.2020.3008668.

72. H. W. Lai, D. Xue, H. Wong, K. K. So, and X. Y. Zhang, "Broadband Circularly Polarized Patch Antenna Arrays With Multiple-Layers Structure," *IEEE Antennas and Wireless Propagation Letters* 16 (2016): 525–528, https://doi.org/10.1109/lawp.2016.2587302.